Bidding Method for EV Aggregators in Flexible Ramping Product Trading Market Considering Charging and Swapping Flexibility Aggregation

Xu Wang, *Senior Member*, *IEEE*, Hanxiao Wu, Guanxun Diao, Chen Fang, Canbing Li, *Senior Member*, *IEEE*, Kai Gong, Chuanwen Jiang, Wentao Huang, *Senior Member*, *IEEE*, and Shenxi Zhang, *Senior Member*, *IEEE*

***Abstract*—Flexible ramping product (FRP) trading has emerged as a highly effective solution to cope with the volatility and uncertainty introduced by the increasing integration of renewable energy sources. This paper proposes a bidding method for electric vehicle aggregators (EVAs) in the FRP trading market. To effectively articulate the spatiotemporal operational characteristics intrinsic to EVAs, a charging and swapping flexibility aggregation model is formulated. The model is developed by accurately simulating the charging and swapping demands of plug-in electric vehicles and battery-swapping electric vehicles in different charging modes. A novel bilevel optimization model is developed to address the conflicting objectives in the FRP trading market between the EVAs and electric vehicles (EVs), aiming to optimize the incentive prices and charging strategies. The upper level optimizes the bidding profits of EVAs, whereas the lower level models the EV charging behavior using the charging and swapping flexibility aggregation model. To solve the high computational complexity of the high-dimensional nonconvex optimization problem owing to the vast number of EVs, a data-driven evolutionary algorithm incorporated with a zebra optimization algorithm is adopted. Owing to the limited data available for training high-quality agent models in real scenarios, a semi-supervised learning-based tri-training algorithm is adopted to enhance the efficiency of data utilization. Case studies validate the effectiveness of the proposed method.**

***Index Terms*—Electric vehicle aggregator, electric vehicle, flexible ramping product, electricity market, flexibility, charging, swapping.**

I. Introduction

As China progresses toward its goals of "carbon emission peaking and carbon neutrality" the total installed capacity of wind, solar, and other renewable energy sources is expected to exceed 1.2 TW by 2030 [1]. The inherent intermittency and volatility of integrated renewable energy sources have inevitably led to an increasing demand for enhanced power system regulations. Improving the power system flexibility is an urgent priority. To address the fluctuations in the net load, the power system requires sufficient flexible ramping capability. In response, two major regional transmission system operators in the United States, California Independent System Operator (CAISO) and Midcontinent Independent System Operator (MISO), designed flexible ramping products (FRPs) to mitigate potential ramping capacity shortages [2]. On April 15, 2020, the North China Branch of State Grid Corporation of China officially incorporated vehicle-to-grid (V2G) charging pile resources into the North China power peak-shaving ancillary service market for a formal settlement [3]. In March 2024, the "Shandong Electric Power Ramp-up Auxiliary Service Market Trading Rules (Trial)" were officially implemented, with suppliers of ramp-up auxiliary services including independent auxiliary service providers such as independent renewable energy storage stations [4]. A key participant in the flexible ramping market is the energy storage system. Similar to energy storage, electric vehicles (EVs) also have the capability to participate in the flexible ramping market. Relevant studies examined the participation of EVs in the flexible ramping market [5].

In recent years, EVs have emerged as a major trend in sustainable transportation owing to their notable advantages, including reduced carbon emissions, positive environmental impacts, and lower energy costs. Once connected to the power grid, EV batteries can be charged and discharged, effectively functioning as distributed energy storage resources. Relevant literature on the participation of EVs in power grid regulation and EV charging management, considering the willingness of EV owners, is provided in Supplementary Material A.

The battery is a critical factor that influences the charging

Manuscript received: April 21, 2025; revised: July 20, 2025; accepted: August 18, 2025. Date of CrossCheck: August 18, 2025. Date of online publication: September 18, 2025.

This work was supported in part by the National Natural Science Foundation of China (No. 52277110), the National Key Research and Development Program of China (No. 2023YFE0119800), and Soft Science Research Project of Science and Technology Commission of Shanghai Municipality (No. 25692109900). This research was supported by Qizhen Chen, Ke Zhang, and Jun Ke, to whom all authors express sincere gratitude.

X. Wang (corresponding author), H. Wu, C. Li, C. Jiang, W. Huang, and S. Zhang are with the Key Laboratory of Control of Power Transmission and Conversion (Shanghai Jiao Tong University), Ministry of Education, Shanghai 200240, China (e-mail: wangxu1989@sjtu. edu. cn; chongjingzhedewuhx@sjtu. edu.cn; licanbing@sjtu.edu.cn; jiangcw@sjtu.edu.cn; hwt8989@sjtu.edu.cn; willzsx@sjtu.edu.cn).

G. Diao and C. Fang are with State Grid Shanghai Municipal Electric Power Company, Shanghai, China (e-mail: diaoguanxun@163.com; fangc02@139.com).

K. Gong is with Zhejiang University, Hangzhou, China (e-mail: kaigong@zju. edu.cn).

DOI: 10.35833/MPCE.2025.000358

cost of EVs. Reference [6] proposes an EV charging scheduling scheme for parking charging systems that minimizes battery degradation costs by optimizing the charging modes to reduce battery wear and extend battery life. Reference [7] suggests a method to mitigate EV battery degradation by optimizing charging and energy management strategies based on a battery life loss model, reducing aging costs and improving long-term battery performance.

However, the participation of large-scale EVs in the electricity market inevitably requires methods for quantifying their power flexibility. Flexibility aggregation, which represents the power regulation potential of EVs, serves as the foundation for market bidding and capacity declarations for electric vehicle aggregators (EVAs). References [8]-[11] develop a method for evaluating the real-time power regulation capacity of large-scale EVs. This method is designed to support power system frequency regulation by accurately estimating the regulation capacity that EVs can provide under various conditions, thereby enhancing the stability of the power system. To address the challenges of numerous decision variables and constraints in the power flexibility aggregation for large-scale EVs, [12]-[16] explore the use of the power flexibility region method to represent the power regulation capability. This method reduces model dimensionality by aggregating the power flexibility regions of individual EVs into a cluster-level power flexibility region, where the power of the cluster serves as the decision variable in subsequent models.

The aforementioned studies evaluate the flexibility of individual and clustered EVs based on user-agreed charging plans, and further analyze the influences of different charging strategies and application scenarios on the real-time power regulation capacity of clusters. Although these evaluations thoroughly explore the flexibility of EVs, they do not account for the differences between battery swapping and charging/discharging. The physical meanings of battery swapping and charging behaviors in the plug-in charging modes are different. Typically, the former requires the station to satisfy a specific battery quantity requirement at a certain point in time, whereas the latter requires the battery to satisfy a specific state of charge (SOC) at a particular point in time. Consequently, aggregators cannot directly utilize these findings for capacity declarations in the FRP trading market. Therefore, an accurate power flexibility aggregation method is urgently required for large-scale EVs.

Considering the varying flexibilities of EVs, studies on the operational strategies of EVAs participating in the electricity market have gained attention. Adaptive bidding strategies based on a two-stage artificial neural network are proposed in [17]-[19] and are designed to assist EVAs in submitting optimal bids to system operators while satisfying the expected needs of their users. These strategies enable aggregators to make accurate decisions in the electricity market. References [20] and [21] develop uncertainty response models for generalized energy storage on the demand side and explore how EVA can improve revenue in the ancillary service market by combining EVs with energy storage resources. In addition, a leader-follower game-based approach is formulated to determine the electricity selling price between the virtual power plant and EVs within the aggregator in [22].

In the aforementioned literature, the operational strategies of EVAs ignore fair profit allocations for EVs. Considering the interests of both EVAs and EVs, a bilevel nonconvex optimization problem must be solved. As several EVs are involved in the optimal operation of EVAs, the computational complexity of a lower-level optimization problem for an individual EV is enormous. To address these computational challenges, data-driven methods are applied instead of the traditional model-based optimization methods. The advantages of data-driven methods over traditional model-based optimization methods are presented in Supplementary Material A.

To address these challenges, we propose a bidding method for EVAs to participate in the FRP trading market based on a zebra optimization algorithm (ZOA)-based data-driven evolutionary algorithm (DDEA) using a semi-supervised learning-based tri-training algorithm. The main contributions of this study are as follows.

1) A charging and swapping flexibility aggregation model for EVAs is proposed. For plug-in electric vehicles (PEVs), a charging flexibility aggregation model is developed according to different charging modes, considering battery degradation and incentive prices. For battery-swapping electric vehicles (BSEVs) with varying initial SOCs, a battery swapping model is adopted to ensure continuous battery swapping services (BSSs). Furthermore, a swapping flexibility aggregation model is introduced to capture and quantify the flexibility of BSEVs. The charging and swapping flexibility aggregation model provides flexibility parameters for the EVAs to participate in power regulation.

2) A bilevel optimization model for the bidding method of EVAs is developed to comprehensively incorporate the bidding interests of both EVAs and EVs into the FRP trading market. This model focuses on the commercial behavior of EVAs, including the electricity supply to EVs and the incentivization of their participation in the FRP trading market, thereby enhancing the willingness of EV owners to participate in the market.

3) We propose a ZOA-based DDEA using a semi-supervised learning-based tri-training algorithm to solve the bilevel optimization model. Surrogate models are developed using data-driven methods to replace traditional model-based optimization methods, and their quality, which is limited by data availability, is enhanced using a semi-supervised learning-based tri-training algorithm. The proposed algorithm reduces the computational burden and improves data utilization efficiency, achieving high computational accuracy even with limited data.

The remainder of this paper is organized as follows. Section II proposes a charging and swapping flexibility aggregation model for EVAs. Section III presents the bidding method for EVAs in the FRP trading market. Section IV provides a detailed introduction to the ZOA-based DDEA using a semi-supervised learning-based tri-training algorithm. Section V presents case studies, and Section VI concludes this paper.

II. CHARGING AND SWAPPING FLEXIBILITY AGGREGATION MODEL FOR EVAS

EVs can actively participate in the power system dispatch through V2G technology. Generally, an EVA consists of several battery swapping and charging stations (BSCSs). In a BSCS, EV charging and battery swapping are accommodated simultaneously. This study considers both battery charging and swapping modes with a focus on the differences in the flexibility inherent to each mode. The differences in flexibility between PEVs and BSEVs are presented in Supplementary Material B. To accurately reflect their actual response capabilities, we evaluate the flexibility characteristics of PEVs and BSEVs separately in the modeling and analysis processes.

A. EV Charging Model for PEVs

The response behaviors and capabilities of PEVs are directly influenced by their flexibility. The expansion of the feasible charging/discharging power regulation of PEVs reflects a broader SOC range, transitioning from the initial state to the target state under feasible dispatch strategies. This, in turn, enhances the flexibility in power regulation. The state vector $\boldsymbol{S}_{evcs}=[E_{start},E_{exp},E_{ms},t_{start},t_{end}]$ is used to represent the energy constraints for the flexibility of the PEVs. The dimensions correspond to the SOC at the time of entry E_{start}, expected SOC at the time of departure E_{exp}, the minimum SOC required to satisfy the next travel demand E_{ms}, entry time t_{start}, and expected departure time t_{end}.

PEVs are typically reluctant to voluntarily engage in the charging/discharging management of stations. Therefore, an appropriate incentive mechanism should be implemented to encourage the participation of PEVs in demand response. To account for the differences in battery degradation among various PEVs, we categorize the charging modes into three types. The SOC boundaries for each mode are presented in the Supplementary Material C Fig. SC1. Given the variations in the incentive prices, the current charging mode may be subject to switching. Additionally, to satisfy the travel requirements of PEVs, the charging station must first charge the EV to its required energy level E_{ms} upon connection to the grid before controlling the charging/discharging behavior for the demand response. This ensures that the participation of PEVs in demand response does not interfere with travel requirements. The charging modes are described in detail below.

1) Charging Mode I

The PEV charges only after it is connected to the grid. The charging station is only authorized to delay the charging time of the PEVs and cannot change the charging power. This mode exhibits a relatively limited response capability but has a minimal influence on the battery. This is associated with lower incentive prices. The charging power boundary constraints are given as:

$$P_j^{\mathrm{I}}(t)=\Gamma_{ch,j}^{\mathrm{I}}(t)P_{L,j}^{\mathrm{I}}(t)\eta_L \tag{1}$$

$$P_{L,j}^{\mathrm{I}}(t)=P_{L,j}^{\mathrm{I,max}} \tag{2}$$

$$E_{j,\min}^{\mathrm{I}}(t)=\begin{cases}E_{j,ms}^{\mathrm{I}} & t_{start}\le t<t_{ab}\\ E_{j,exp}^{\mathrm{I}}-(t_{end}-t)\eta_L P_{L,j}^{\mathrm{I,max}} & t_{ab}\le t\le t_{end}\end{cases} \tag{3}$$

$$t_{ab}=t_{end}-(E_{j,exp}^{\mathrm{I}}-E_{j,ms}^{\mathrm{I}})/(P_{L,j}^{\mathrm{I,max}}\eta_L) \tag{4}$$

$$E_j^{\mathrm{I}}(t)=E_j^{\mathrm{I}}(t-1)+P_j^{\mathrm{I}}(t) \tag{5}$$

$$t_{ms}=(E_{j,ms}^{\mathrm{I}}-E_{j,start}^{\mathrm{I}})/(P_{L,j}^{\mathrm{I,max}}\eta_L) \tag{6}$$

where $P_j^i(t)$ is the real-time net charging power of PEV j at time t in mode i; $P_{L,j}^i(t)$ is the real-time charging power of PEV j at time t in mode i; $\Gamma_{ch,j}^i(t)$ is the binary decision variable controlling the charging behavior of PEV j in mode i; $P_{L,j}^{i,\max}$ is the upper limit of the charging power of PEV j in mode i; $E_j^i(t)$ is the SOC of PEV j at time t in mode i; $E_{j,\min}^i(t)$ is the minimum SOC of PEV j at time t in mode i; $E_{j,ms}^i$ is the minimum SOC required to meet the next travel demand of PEV j in mode i; $E_{j,exp}^i$ is the expected SOC at the time of departure of PEV j in mode i; $E_{j,start}^i$ is the SOC at the time of entry of PEV j in mode i; t_{ab} is the controllable start time for PEV j; η_L is the charging efficiency; and t_{ms} is the uncontrollable duration for PEVs. To facilitate the analysis, the charging and discharging processes are discretized by dividing each cycle into multiple time intervals.

2) Charging Mode II

The PEV connected to the grid exhibits adjustable charging power. Once connected, the PEV remains in at locked state and cannot be disconnected from the grid at a designated time. Because of the moderate response capability of PEVs, this mode receives a mid-tier incentive price. The charging power boundary constraints are given as:

$$P_j^{\mathrm{II}}(t)=\Gamma_{ch,j}^{\mathrm{II}}(t)P_{L,j}^{\mathrm{II}}(t)\eta_L \tag{7}$$

$$\begin{cases}0\le P_j^{\mathrm{II}}(t)\le P_{L,j}^{\mathrm{II,max}}\eta_{\mathrm{L}} & E_j^{\mathrm{II}}(t)\ge E_{j,ms}^{\mathrm{II}}\\ \theta_{dis}^{\mathrm{II}}\le P_j^{\mathrm{II}}(t)\le P_{L,j}^{\mathrm{II,max}}\eta_{\mathrm{L}} & E_j^{\mathrm{II}}(t)<E_{j,ms}^{\mathrm{II}}\end{cases} \tag{8}$$

$$\theta_{dis}^{\mathrm{II}}=(E_{j,exp}^{\mathrm{II}}-E_{j,start}^{\mathrm{II}})/(t_{end}-t_{start}) \tag{9}$$

$$E_{j,\min}^{\mathrm{II}}(t)=\begin{cases}E_{j,start}^{\mathrm{II}}+\theta_{dis}(t-t_{start}) & t_{start}\le t<t_{ms}\\ E_{j,ms}^{\mathrm{II}} & t_{ms}\le t<t_{ab}\\ E_{j,exp}^{\mathrm{II}}-P_{L,j}^{\mathrm{II,max}}\eta_L(t_{end}-t) & t_{ab}\le t\le t_{end}\end{cases} \tag{10}$$

$$t_{ab}=t_{end}-(E_{j,exp}^{\mathrm{II}}-E_{j,ms}^{\mathrm{II}})/(P_{L,j}^{\mathrm{II,max}}\eta_L) \tag{11}$$

$$E_j^{\mathrm{II}}(t)=E_j^{\mathrm{II}}(t-1)+P_j^{\mathrm{II}}(t) \tag{12}$$

$$t_{ms}=t_{start}+(E_{j,ms}^{\mathrm{II}}-E_{j,start}^{\mathrm{II}})/\theta_{dis}^{\mathrm{II}} \tag{13}$$

where θ_{dis}^i is an intermediate variable used to calculate t_{ms}, denoting the slope of the line connecting the initial SOC $E_{j,start}^i$ and expected SOC $E_{j,exp}^i$ in mode i.

3) Charging Mode III

Once connected to the grid, the PEV remains locked and cannot disconnect from the grid at a designated time. In this mode, PEVs can charge or discharge while simultaneously regulating their charging and discharging power, exhibiting exceptional response capabilities. However, frequent charging and discharging lead to higher battery degradation. Therefore, the incentive price for this mode is the highest among the three modes. Its boundary constraints differ from those in Mode II, replacing constraints (7) and (8) in Mode II with (14)-(17), forming the boundary constraints for Mode III.

$$P_j^{\mathrm{III}}(t)=\Gamma_{ch,j}^{\mathrm{III}}P_{L,j}^{\mathrm{III}}(t)\eta_L-\Gamma_{dis,j}^{\mathrm{III}}P_{G,j}^{\mathrm{III}}(t)/\eta_G \tag{14}$$

$$\begin{cases} 0 \le P_{L,j}^{\mathrm{III}}(t) \le P_{L,j}^{\mathrm{III,max}} \\ 0 \le P_{G,j}^{\mathrm{III}}(t) \le P_{G,j}^{\mathrm{III,max}} \end{cases} \quad E_j^{\mathrm{III}}(t) \ge E_{j,ms}^{\mathrm{III}} \tag{15}$$

$$\theta_{dis}^{\mathrm{III}} \le P_j^{\mathrm{III}}(t) \le P_{L,j}^{\mathrm{III,max}} \eta_L \quad E_j^{\mathrm{III}}(t) < E_{j,ms}^{\mathrm{III}} \tag{16}$$

$$P_{L,j}^{\mathrm{III}}(t) P_{G,j}^{\mathrm{III}}(t) = 0 \tag{17}$$

where $\Gamma_{dis,j}^{i}(t)$ is the binary decision variable controlling the discharging behavior of PEV j in mode i; $P_{G,j}^{i}(t)$ is the real-time discharging power of PEV j at time t in mode i; $P_{G,j}^{i,\max}$ is the upper limit of the discharging power of PEV j in mode i; and η_G is the discharging efficiency.

B. Charging Flexibility Aggregation Model for PEVs

In this study, the three charging modes correspond to different types of charging piles, as shown in Supplementary Material C Table SCI. Evaluating the flexibility of PEVs is of substantial significance for EVAs in setting the incentive price to optimize demand response.

The power flexibility evaluation consists of two steps. First, the charging/discharging load curves of the PEVs are calculated by minimizing the associated cost. The power flexibility of the PEVs is evaluated by comparing the feasible boundary of the SOC and the charging/discharging power bounds. The load curve calculation of the PEVs aims to minimize their charging/discharging costs based on the charging price and incentive price, which is formulated as:

$$\min B_{j,EV} = C_1 + C_2 - \gamma_{\mathrm{I}} \beta_c^{\mathrm{I}} - \gamma_{\mathrm{II}} \beta_c^{\mathrm{II}} - \gamma_{\mathrm{III}} \beta_c^{\mathrm{III}} \tag{18}$$

$$C_1 = \sum_{t=t_{start}}^{t_{end}} (P_{L,j}^{i}(t) - P_{G,j}^{i}(t)) \lambda_t^{\mathrm{tr}} \quad \forall i \in \{\mathrm{I}, \mathrm{II}, \mathrm{III}\} \tag{19}$$

$$C_2 = \sum_{t=t_{start}}^{t_{end}} (\Gamma_{ch,j}^{i}(t) + \Gamma_{dis,j}^{i}(t)) \pi_c^{i} \quad \forall i \in \{\mathrm{I}, \mathrm{II}, \mathrm{III}\} \tag{20}$$

$$\gamma_{\mathrm{I}} + \gamma_{\mathrm{II}} + \gamma_{\mathrm{III}} = 1 \tag{21}$$

where C_1 is the charging cost of the PEVs; C_2 is the charging and discharging loss of the battery; β_c^i is the incentive price in mode i; γ_i is the binary variable indicating whether the PEV is in mode i; λ_t^{tr} is the electricity price of the charging station at time t; and π_c^i is the quantified price of the charging and discharging losses of the battery in mode i with the assumption that $\pi_c^{\mathrm{III}} > \pi_c^{\mathrm{II}} > \pi_c^{\mathrm{I}}$.

Additionally, to protect the battery, the numbers of charging cycles $N_{ch,j}$ and discharging cycles $N_{dis,j}$ are restricted as:

$$\begin{cases} \sum_{t=t_{\mathrm{start}}}^{t_{\mathrm{end}}} \Gamma_{ch,j}^{i}(t) \le N_{ch,j} & \forall i \in \{\mathrm{I}, \mathrm{II}, \mathrm{III}\} \\ \sum_{t=t_{\mathrm{start}}}^{t_{\mathrm{end}}} \Gamma_{dis,j}^{i}(t) \le N_{dis,j} & \forall i \in \{\mathrm{III}\} \end{cases} \tag{22}$$

The power flexibility of the individual PEV is then evaluated by:

$$\bar{P}_{j,c}(t) = \max\{\min[\bar{P}_{j,\alpha}(t), \bar{P}_{j,\beta}(t)], 0\} \tag{23}$$

$$\bar{P}_{j,\alpha}(t) = P_{G,j}^{i,\max} + (P_{L,j}^{i}(t) - P_{G,j}^{i}(t)) \quad \forall i \in \{\mathrm{I}, \mathrm{II}, \mathrm{III}\} \tag{24}$$

$$\bar{P}_{j,\beta}(t) = (E_j^{i}(t) - E_{j,\min}^{i}(t+1)) \eta_L^{-1} + (P_{L,j}^{i}(t) - P_{G,j}^{i}(t)) \quad \{\forall i \in \mathrm{I}, \mathrm{II}, \mathrm{III}\} \tag{25}$$

$$\underline{P}_{j,c}(t) = \max\{\min[\underline{P}_{j,\alpha}(t), \underline{P}_{j,\beta}(t)], 0\} \tag{26}$$

$$\underline{P}_{j,\alpha}(t) = P_{L,j}^{i,\max} - (P_{L,j}^{i}(t) - P_{G,j}^{i}(t)) \quad \forall i \in \{\mathrm{I}, \mathrm{II}, \mathrm{III}\} \tag{27}$$

$$\underline{P}_{j,\beta}(t) = (E_{j,\max}^{i}(t+1) - E_j^{i}(t)) \eta_L^{-1} - (P_{L,j}^{i}(t) - P_{G,j}^{i}(t)) \quad \forall i \in \{\mathrm{I}, \mathrm{II}, \mathrm{III}\} \tag{28}$$

where $\bar{P}_{j,c}(t)$ and $\underline{P}_{j,c}(t)$ are the maximum discharging and charging capacities of PEV j at time t, respectively; $\bar{P}_{j,\alpha}(t)$ is the maximum discharging capacity of PEV j at time t constrained by the maximum discharging power limit; $\bar{P}_{j,\beta}(t)$ is the maximum discharging capacity of PEV j at time t constrained by the minimum energy limit; $\underline{P}_{j,\alpha}(t)$ is the maximum charging capacity of PEV j at time t constrained by the maximum charging power limit; and $\underline{P}_{j,\beta}(t)$ is the maximum charging capacity of PEV j at time t constrained by the maximum energy limit. Thus, the power flexibility of the PEVs is obtained as:

$$\bar{P}_{t,i}^{\mathrm{PEV}} = \sum_{j=1}^{J} \bar{P}_{j,c}(t) \tag{29}$$

$$\underline{P}_{t,i}^{\mathrm{PEV}} = \sum_{j=1}^{J} \underline{P}_{j,c}(t) \tag{30}$$

where $\bar{P}_{t,i}^{\mathrm{PEV}}$ and $\underline{P}_{t,i}^{\mathrm{PEV}}$ are the maximum discharging and charging capacities of the PEVs in the BSCS i at time t, respectively; and J is the number of PEVs.

C. Battery Swapping Model for BSEVs

As economic commodities, battery packs provide energy replenishment for EV users. BSEV users expect to receive fully charged battery packs during battery swapping. Therefore, the SOC at the end of the charging process should be carefully regulated, i. e., $E_{exp} = E_{\max}$, where $E_{\max}$ denotes the maximum SOC that a battery pack can reach, corresponding to its fully charged capacity. To determine the controllable state of spare battery packs, the following assumptions are made: ① the charging rate of the battery pack remains constant over each unit time interval; ② the state information of the battery pack is known upon removal from the EV; ③ charging ceases only when the battery pack reaches full capacity, although the system can delay the start of the charging process; ④ the battery swapping time is neglected.

In general, BSEV users visit a battery swapping station when the SOC of the batteries drops to a certain level (approximately 20%-30%) to avoid complete depletion, which would prevent further driving. However, in some cases, users may choose to visit a station when a significant amount of battery charge remains (e.g., users with higher range anxiety) to ensure safe and stable driving.

In this study, the SOCs of the batteries are divided into M intervals: $[S_{OC,0}, S_{OC,1}]$, $[S_{OC,1}, S_{OC,2}]$, …, $[S_{OC,M-1}, S_{OC,M}]$, where $S_{OC,0}$ and $S_{OC,M}$ are the minimum and maximum SOC values, respectively. The length of each SOC interval ΔS_{OC} is identical. Batteries in the last interval of $[S_{OC,M-1}, S_{OC,M}]$ are considered available spare batteries, whereas batteries in other intervals may include recently swapped low-charge batteries. After the battery is charged for a certain time period, its SOC shifts to the adjacent interval. For example, a battery in interval $[S_{OC,i}, S_{OC,i+1}]$ at time t, after being charged for time ΔT,

transitions to interval $[S_{OC,i+1}, S_{OC,i+2}]$ at time $t+1$. We then use the variables $N_{1,s,t}, N_{2,s,t}, \ldots, N_{M,s,t}$, $N_{1,c,t}, N_{2,c,t}, \ldots, N_{M,c,t}$, and $N_{1,d,t}, N_{2,d,t}, \ldots, N_{M,d,t}$ to denote the number of batteries in all SOC states, the number of batteries being charged, and the number of batteries being swapped out, respectively, corresponding to the intervals $[S_{OC,0}, S_{OC,1}]$, $[S_{OC,1}, S_{OC,2}]$, and $[S_{OC,M-1}, S_{OC,M}]$ at time t.

Assume that the number of batteries in each SOC state at the initial time $t=0$ equals that of available spare batteries. The changes in the number of batteries across different SOC intervals can be expressed by:

$$\begin{cases} N_{1,s,t} = N_{1,s,t-1} - N_{1,c,t} + N_{1,d,t} \\ N_{2,s,t} = N_{2,s,t-1} + N_{1,c,t} - N_{2,c,t} + N_{2,d,t} \\ \vdots \\ N_{M-1,s,t} = N_{M-1,s,t-1} + N_{M-2,c,t} - N_{M-1,c,t} + N_{M-1,d,t} \\ N_{M,s,t} = N_{M,s,t-1} + N_{M-1,c,t} - \sum_{m=0}^{M-1} N_{m,d,t} \end{cases} \tag{31}$$

To ensure the continuous and normal operation of the BSCS, the following constraints must be satisfied:

$$N_{all,c,t} = \sum_{m=1}^{M-1} N_{m,c,t} \tag{32}$$

$$0 \le N_{m,c,t} \le N_{m,s,t-1} \quad m = 1, 2, \ldots, M-1 \tag{33}$$

$$0 \le N_{all,c,t} \le N_{\max,sw} \tag{34}$$

$$N_{M,s,t} \ge \sum_{m=0}^{M-1} N_{m,d,t+1} \tag{35}$$

$$\sum_{m=1}^{M} m\Delta S_{OC} \left| N_{m,s,0} - N_{M,s,T} \right| \le \Delta S_{OC,\max} \tag{36}$$

where $N_{all,c,t}$ is the total number of batteries charged within the station at time t; $N_{\max,sw}$ is the number of battery swapping devices; $N_{m,s,0}$ is the number of batteries in the m^{th} SOC state within the station at time $t=0$; $N_{M,s,T}$ is the number of batteries in the M^{th} SOC state within the station at time $t=T$, and T is the total number of scheduling periods; and $\Delta S_{OC,\max}$ denotes a minor energy deviation. Constraint (33) ensures that the number of batteries charged in each SOC interval does not exceed that of the corresponding SOC interval. Constraint (34) guarantees that the total number of batteries charged during each time period does not exceed $N_{\max,sw}$ in the BSCS. Constraint (35) ensures that fully charged batteries during each time period can satisfy the battery swapping demand during the subsequent time period. In (36), the total energy of all the batteries at the initial time and final time can only have a minimal deviation $\Delta S_{OC,\max}$, allowing the BSCS to operate continuously.

D. Swapping Flexibility Aggregation Model for BSEVs

To evaluate the power flexibility of BSEVs, the focus is on determining the upper and lower power boundaries that satisfy the operational requirements of the BSS. From the perspective of the BSS, if the charging/discharging power remains within the range mentioned above, the battery swapping demands during each time period and the subsequent operational requirements can be ensured. However, one of the challenges in identifying the power flexibility boundaries is the complex state transitions of spare batteries within the BSS. The precondition for the BSS to provide power regulation capacity is to fully utilize its spare batteries, delaying the charging of spare batteries while satisfying the demands of battery swapping.

Therefore, the lower power flexibility boundary of the BSS is described as delaying the charging of partially spare batteries while satisfying the battery swapping demands during each time period to minimize the number of batteries being charged during each time period. The upper power flexibility boundary of the BSS is constrained by the numbers of available charging devices and uncharged spare batteries, and is linearly related to the minimum value of the two.

In this study, the power flexibility evaluation of the BSS is extended from solving within a single battery interval to solving across an entire range of battery intervals. Let $x(t)$ represent the number of batteries that start charging at time t after being swapped in the BSS, $x'(t)$ represent the number of batteries that are fully charged at time t, $y(t)$ represent the remaining number of available spare batteries, $a(t)$ represent the cumulative number of batteries being charged, $b(t)$ represent the number of spare batteries with delayed charging, and $D(t)$ represent the number of batteries being swapped at time t. The objective is to minimize the total number of spare batteries available for swapping over all time periods, thereby achieving the minimum charging load while meeting the swapping demand. Thus, the lower power flexibility boundary evaluation problem can be modeled as:

$$\min \sum_{t \in T} y(t) \tag{37}$$

$$0 \le x(t) \le N_{\max,sw} \tag{38}$$

$$0 \le x'(t) \le D(t) \tag{39}$$

$$0 \le y(t) \le y(0) \tag{40}$$

$$y(t) = y(0) - a(t) - b(t) \quad t \in (0, T] \tag{41}$$

$$a(t) = \sum_{i=0}^{t} (x(i) - x'(i)) \tag{42}$$

$$b(t) = \sum_{i=0}^{t} (D(i) - x(i)) \tag{43}$$

Constraints (38)-(40) are the upper and lower limits of the spare batteries, where $x(t)$ and $x'(t)$ must be less than or equal to the battery swapping demand at time t, and $y(t)$ should not exceed that of spare batteries. Constraint (41) states that the number of available spare batteries at time t equals that of spare batteries minus the sum of the batteries currently being charged and the fully depleted batteries not being charged. Constraint (42) indicates that the total number of batteries charged at time t is obtained by summing that of newly swapped and immediately charged batteries minus the number of batteries that have recently been fully charged. Similarly, constraint (43) represents the total number of swapped batteries that remain uncharged and is calculated as the difference between the total battery swapping demand before time t and the number of batteries swapped or

immediately charged.

The value of $x'(t)$ depends on the time required to fully charge the spare batteries in the current SOC interval. Taking the batteries in the SOC interval [0.2, 0.3] as an example, assuming that the time required to charge them from 20% to 90% is T_{need}, these newly swapped batteries will not be available until at least time $t=1+T_{need}$. Therefore, $x'(t)$ is given as:

$$x'(t)=\begin{cases}0 & t\le T_{need}\\ x(t-T_{need}) & t>T_{need}\end{cases} \tag{44}$$

By solving the above minimum reserve charging load optimization problem, the number of reserve batteries $x(t)$ (the "Min" line in Fig. 1) charged immediately after replacement at each time step, while meeting the battery swapping demands, can be obtained. This optimization problem aims to delay the charging of spare batteries as much as possible while still satisfying the battery swapping demands. Consequently, there will be an accumulation of uncharged swapped batteries, represented by $b(t)$ (the "Max" line in Fig. 1). Charging all the accumulated batteries yields the maximum charging curve. Therefore, the power flexibility capacity provided by the BSS is defined by the range between the minimum and maximum numbers of charging batteries required to satisfy the battery swapping demand, as shown by the light-green area in Fig. 1. In addition, the feasible region of power flexibility for the BSS is further constrained by another boundary. If all swapped batteries begin charging immediately after being swapped out, the curve $c(t)$ (the "instant charging" line in Fig. 1) is formed, where $c(t)$ is the cumulative number of uncharged batteries swapped out at each time. This results in a large charging load at the early stages of the swapping process. A feasible region of power flexibility is obtained, as indicated by the light-orange area in Fig. 1.

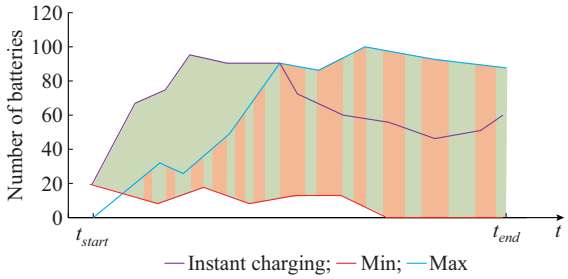

Fig. 1. Schematic of feasible region of power flexibility for BSS.

Let P_{cu}^{BSS} and P_{cd}^{BSS} represent the lower and upper limits of the feasible region of power flexibility for the BSS, respectively. The above process can be described as:

$$\begin{cases}P_{cu}^{\mathrm{BSS}}(t)=\max\{b(t),c(t)\}\cdot P_{rtd}^{\mathrm{BSEV}}\\ P_{cd}^{\mathrm{BSS}}(t)=\min\{x(t),c(t)\}\cdot P_{rtd}^{\mathrm{BSEV}}\end{cases} \tag{45}$$

$$c(t)=\sum_{i=0}^{t}(D(i)-x'(i)) \tag{46}$$

where P_{rtd}^{BSEV} is the rated charging power of spare batteries.

Finally, the following optimization model for determining the lower boundary of the BSS can be formulated as:

$$\min\sum_{t\in T}N_{M,s,t} \tag{47}$$

$$\begin{cases}0\le N_{all,c,t}\le N_{\max,sw} & \forall t\in T\\ 0\le N_{M-1,c,t}\le N_{all,d,t} & \forall t\in T\\ N_{M,s,t}=N_{M,s,0}-\sum_{i=0}^{t}(N_{all,d,i}-N_{M-1,c,i}) & \\ (31)\text{-}(36) & \end{cases} \tag{48}$$

where $N_{all,d,t}$ is the total number of batteries swapped out within the station at time t.

Thus, the upper and lower boundaries of the feasible region of power flexibility for the BSS, considering the division of SOC intervals, can be expressed as $\bar{P}_{t,i}^{\mathrm{BSS}}$ and $\underline{P}_{t,i}^{\mathrm{BSS}}$, respectively.

$$\begin{cases}\bar{P}_{t,i}^{\mathrm{BSS}}=\max\{N_{all,d,t}-N_{all,c,t},N_{all,d,t}-N_{M-1,c,t}\}\cdot P_{rtd}^{\mathrm{BSEV}}\\ \underline{P}_{t,i}^{\mathrm{BSS}}=\min\{N_{all,c,t},N_{all,d,t}-N_{M-1,c,t}\}\cdot P_{rtd}^{\mathrm{BSEV}}\end{cases} \tag{49}$$

Thus, the corresponding feasible region of power flexibility for the BSS can be determined. Additionally, the complex state dynamics of spare batteries are reduced to a two-dimensional envelope region for more efficient analysis.

III. Bidding Method of EVAs in FRP Trading Market

A. Modeling for Bidding Method of EVAs

This subsection presents a mathematical model for EVAs, which provide various power products externally, supply energy internally, and offer incentives to EV users. The EVA is required to meet the swapping and charging demands of EVs, participating in both the power energy market and the FRP trading market, based on the feasible region of power flexibility of the aggregated PEVs and the swapping batteries in a BSCS. The trading model is presented in Supplementary Material C Fig. SC2.

The model for bidding method of EVAs is formulated as a bilevel optimization model. The upper-level optimization model focuses on the participation of BSCSs in both the energy and FRP trading markets, aiming to maximize profits by purchasing or selling electricity while simultaneously providing FRP services. Assumptions related to the FRP trading market are presented in Supplementary Material D. The decision variable at the upper level is the incentive price offered by BSCSs to EV users. By contrast, the lower-level optimization model is designed to minimize the charging costs of EV users. The upper-level optimization model is formulated as:

$$\max_{\beta_c^{\mathrm{I}},\beta_c^{\mathrm{II}},\beta_c^{\mathrm{III}}}\left\{\sum_{t=1}^{96}(\lambda_t^{\mathrm{tr}}P_t^{\mathrm{D}}-\lambda_t^{\mathrm{mcp}}P_t^{\mathrm{D}}+\lambda_t^{\mathrm{mcu}}P_t^{\mathrm{ru}}+\lambda_t^{\mathrm{mcd}}P_t^{\mathrm{rd}})-\beta_c^{\mathrm{I}}n^{\mathrm{I}}-\beta_c^{\mathrm{II}}n^{\mathrm{II}}-\beta_c^{\mathrm{III}}n^{\mathrm{III}}\right\} \tag{50}$$

$$\beta_{c,\min}^{i}\le\beta_c^{i}\le\beta_{c,\max}^{i}\quad\forall i\in\{\mathrm{I},\mathrm{II},\mathrm{III}\} \tag{51}$$

$$P_t^{\mathrm{D}}=\sum_{i=1}^{n_{\mathrm{BSCS}}}P_{t,i}^{\mathrm{BSCS}} \tag{52}$$

$$P_{t,i}^{\mathrm{BSCS}}=P_{t,i}^{\mathrm{EVCS}}+P_{t,i}^{\mathrm{BSS}} \tag{53}$$

$$-\bar{P}_{t,i}^{\mathrm{BSS}} \le P_{t,i}^{\mathrm{BSS}} \le \underline{P}_{t,i}^{\mathrm{BSS}} \tag{54}$$

$$P_t^{\mathrm{ru}} = \sum_{i=1}^{n} (\bar{P}_{t,i}^{\mathrm{PEV}} + P_{t,i}^{\mathrm{EVCS}} + \bar{P}_{t,i}^{\mathrm{BSS}} + P_{t,i}^{\mathrm{BSS}}) \tag{55}$$

$$P_t^{\mathrm{rd}} = \sum_{i=1}^{n} (\underline{P}_{t,i}^{\mathrm{PEV}} - P_{t,i}^{\mathrm{EVCS}} + \underline{P}_{t,i}^{\mathrm{BSS}} - P_{t,i}^{\mathrm{BSS}}) \tag{56}$$

where λ_t^{mcp} is the clearing price in the energy market; P_t^{D} is the electricity demand declared by the EVA; λ_t^{mcu} and λ_t^{mcd} are the prices for the upward and downward flexibility ramping markets, respectively; P_t^{ru} and P_t^{rd} are the upward and downward FRPs, respectively; n^i is the number of EVs in mode i; $\beta_{c,\min}^i$ and $\beta_{c,\max}^i$ are the lower and upper limits of the incentive price in mode i, respectively; $P_{t,i}^{\mathrm{EVCS}}$ and $P_{t,i}^{\mathrm{BSS}}$ are the loads of PEVs and BSEVs in mode i, respectively; $P_{t,i}^{\mathrm{BSCS}}$ is the load of BSCS in mode i; and n^{BSCS} is the number of BSCSs. Here, $P_{t,i}^{\mathrm{EVCS}}$, $\bar{P}_{t,i}^{\mathrm{EVCS}}$, and $\underline{P}_{t,i}^{\mathrm{EVCS}}$ are determined using the lower-level optimization model.

The lower-level optimization model aims to maximize the benefits of EV users by minimizing charging costs while satisfying their energy demands. The mathematical formulation of the model is presented in (18)-(21).

B. Motivation of DDEA

In general, bilevel optimization problems are solved using Karush-Kuhn-Tucker (KKT) conditions [23]-[25] or intelligent algorithms such as genetic algorithms (GAs) [26]. The application of KKT conditions is based on the assumption that the lower-level optimization model is a convex optimization problem [27]. However, as both the upper- and lower-level optimization models contain integer variables, they fall into the category of mixed-integer nonlinear programming problems, which are inherently nonconvex. Therefore, it is difficult to obtain an optimal solution using KKT conditions. Moreover, owing to the large number of EVs under the management of the EVA, solving the lower-level optimization problem for each EV user results in a substantial computational burden. This complexity makes it impractical to efficiently use either KKT conditions or intelligent algorithms. Given these limitations, traditional model-based optimization methods are unsuitable for this bilevel optimization model. An alternative is to leverage data-driven methods that offer greater flexibility and scalability. Among these methods, the DDEA is regarded as an effective solution for addressing the computational complexity and nonconvexity of the problem. The necessity of adopting the semi-supervised learning-based tri-training algorithm is presented in Supplementary Material D.

IV. ZOA-based DDEA Using Semi-supervised Learning-based Tri-training Algorithm

Intelligent optimization algorithms have been proposed for several years, and their applications across various fields have reached a high level of maturity. In these algorithms, the evaluation of the fitness function constitutes an essential element for determining the search direction. However, in practice, the fitness functions of several optimization problems are difficult to model accurately, which limits the scope of intelligent algorithm applications. To address this limitation, the surrogate model technology has gained attention and has been seamlessly integrated with intelligent optimization algorithms, resulting in surrogate-assisted evolutionary algorithms [28]. As surrogate models are constructed using historical data, they are also referred to as DDEAs.

The accuracy of the surrogate models is closely related to the amount of data available. Tri-training employs the concept of semi-supervised learning [29], which can substantially reduce data requirements while improving accuracy, even when using the same amount of data. Therefore, this paper utilizes a ZOA-based DDEA using the semi-supervised learning-based tri-training algorithm to optimize the accuracy and generalization performance of the surrogate models under limited data conditions, and its flowchart is shown in Supplementary Material E Fig. SE1. The advantages of the ZOA are provided in Supplementary Material E.

A. Process of Proposed Algorithm

Owing to limited data, studies on DDEAs have focused on constructing accurate surrogate models with minimal data, using methods such as polynomial regression [30], artificial neural network [31]-[33], and radial basis function network (RBFN) [34]-[36]. In particular, the RBFN, which is based on interpolation methods, has been widely used owing to its low computational cost and high training speed, particularly for handling large numbers of decision variables [37]. The details of the RBFN are provided in Supplementary Material F.

In the proposed bilevel optimization model, the offline dataset is initially divided into three subsets, denoted as L_1, L_2, and L_3, respectively, used for training the RBFN models M_1, M_2, and M_3. The models take incentive prices as input and the profit of EVAs as output. The objective of training the RBFN models is to accurately capture the functional relationship between the incentive price and the profit of EVAs.

After the RBFN models are trained, a population-based intelligent optimization algorithm such as particle swarm optimization (PSO) or GA is employed to search for an incentive price set that maximizes the profit of EVAs. Q individuals in current population P are represented by $p^1, p^2, ..., p^Q$, and each individual in the current population P is predicted by three trained RBFN models M_1, M_2, and M_3, whose predicted fitness values are denoted by $F_1^1, F_2^1, F_3^1, ..., F_1^Q, F_2^Q, F_3^Q$. Considering the profit of EVAs, we define the fitness function as:

$$F = \sum_{t=1}^{96} (\lambda_t^{\mathrm{tr}} P_t^{\mathrm{D}} - \lambda_t^{\mathrm{mcp}} P_t^{\mathrm{D}} + \lambda_t^{\mathrm{mcu}} P_t^{\mathrm{ru}} + \lambda_t^{\mathrm{mcd}} P_t^{\mathrm{rd}}) - \beta_c^{\mathrm{I}} n^{\mathrm{I}} - \beta_c^{\mathrm{II}} n^{\mathrm{II}} - \beta_c^{\mathrm{III}} n^{\mathrm{III}} \tag{57}$$

Typically, the fitness of each individual in the population is evaluated by substituting the corresponding incentive prices into the proposed bilevel optimization model to obtain the profit of EVAs. To avoid the computational burden of this process, we directly input the incentive prices into the trained RBFN model to estimate the profit of EVAs.

Given the limited availability of data, it is necessary to

augment the original dataset with additional high-confidence data to enhance model training. According to (58), the individual x_i with the highest confidence in P, whose index is S, is selected to enrich L_i, which is based on the prediction difference between the other two models M_j and M_k.

$$S=\underset{1\le S\le Q}{\arg\min}\left(|F_j^S-F_k^S|\right)\quad i,j,k=1,2,3,i\neq j\neq k \tag{58}$$

where F_j^S and F_k^S are the fitness values of the population individual with index S, evaluated by models M_j and M_k, respectively.

Pseudo label $\hat{y}_i$ is the average prediction value of M_j and M_k:

$$\hat{y}_i=\frac{1}{2}(F_j^S+F_k^S)\quad i,j,k=1,2,3,i\neq j\neq k \tag{59}$$

The pseudo label data for M_i are denoted as $(x_i,\hat{y}_i)$. The training dataset L_i is then updated as L_i' by adding $(x_i,\hat{y}_i)$ as follows:

$$L_i'=L_i\cup(x_i,\hat{y}_i) \tag{60}$$

After obtaining $(x_1,\hat{y}_1)$, $(x_2,\hat{y}_2)$, and $(x_3,\hat{y}_3)$ to update L_1, L_2, and L_3, the three RBFN models M_1, M_2, and M_3 are retrained for the surrogate ensemble.

Finally, the fitness of each individual in the population is evaluated using the model integrated from three RBFN models.

B. Process of ZOA

Intelligent optimization algorithms are commonly employed to address optimization problems formulated within the framework of DDEA, with PSO and GA as representative examples. However, the PSO and GA often fall into local optima. In contrast, the ZOA demonstrates a stronger optimization capability owing to its advantages in balancing exploration and exploitation, as well as maintaining population diversity. ZOA is a population-based optimization technique in which each zebra represents a candidate solution. The initial population is randomly distributed within a search space. Mathematically, the position of each zebra is represented by a vector, and the entire population is expressed as:

$$\boldsymbol{X}=[\boldsymbol{X}_1,\boldsymbol{X}_2,\ldots,\boldsymbol{X}_N]^{\mathrm{T}} \tag{61}$$

where $\boldsymbol{X}_i$ is the position of the i^{th} zebra with a dimension of $1\times m$, and m is the number of decision variables; and N is the population size.

The objective function $F(\boldsymbol{X})$ evaluates the position of each zebra, and the resulting fitness values are expressed as:

$$\boldsymbol{F}=[F_1,F_2,\ldots,F_N]^{\mathrm{T}}=[F(\boldsymbol{X}_1),F(\boldsymbol{X}_2),\ldots,F(\boldsymbol{X}_N)]^{\mathrm{T}} \tag{62}$$

In the foraging phase, zebras adjust their movements based on the position of the leading zebra, which represents the current optimal solution within the population. The other zebras update their positions as:

$$x_{i,j}^{\text{new, P1}}=x_{i,j}+r(PZ_j-Ix_{i,j}) \tag{63}$$

where $x_{i,j}^{\text{new, P1}}$ is the new position of the i^{th} zebra in the j^{th} dimension based on the first phase; $x_{i,j}$ is the value for the j^{th} problem variable proposed by the i^{th} zebra; PZ_j is the position of the leading zebra in the j^{th} dimension; r is a random number in the range [0,1]; and I is an integer parameter used to adjust the movement amplitude of the population.

The new position is accepted based on the following conditions:

$$\boldsymbol{X}_i=\begin{cases}\boldsymbol{X}_i^{\text{new, P1}} & F_i^{\text{new, P1}}<F_i\\ \boldsymbol{X}_i & \text{else}\end{cases} \tag{64}$$

where $\boldsymbol{X}_i^{\text{new, P1}}$ is the new status of the i^{th} zebra based on the first phase; and $F_i^{\text{new, P1}}$ is the fitness value of $\boldsymbol{X}_i^{\text{new, P1}}$.

In the second phase, zebras adopt defense strategies based on a predator attack approach. There are two defense strategies: fleeing and collective defense strategies. Let P represent the probability of a zebra choosing the fleeing defense strategy and $1-P$ represent the probability of the zebra adopting the collective defense strategy.

Fleeing defense strategy: when zebras implement a fleeing defense strategy when threatened by large predators such as lions, the corresponding mathematical model is expressed as:

$$x_{i,j}^{\text{new, P2}}=x_{i,j}+R(2r-1)(1-t_c/T_i)x_{i,j} \tag{65}$$

where $x_{i,j}^{\text{new, P2}}$ is the new position of the i^{th} zebra in the j^{th} dimension based on the second phase; R is a constant set to be 0.01; t_c is the current number of iterations; and T_i is the maximum number of iterations.

Collective defense strategy: when zebras encounter smaller predators such as hyenas or wild dogs, they employ a collective defense strategy by gathering for protection. The mathematical model for this strategy is expressed as:

$$x_{i,j}^{\text{new, P2}}=x_{i,j}+r(AZ_j-Ix_{i,j}) \tag{66}$$

where AZ_j is the position of the attacked zebra in the j^{th} dimension.

The position updated from the defense strategies is accepted based on the following conditions:

$$\boldsymbol{X}_i=\begin{cases}\boldsymbol{X}_i^{\text{new, P2}} & F_i^{\text{new, P2}}<F_i\\ \boldsymbol{X}_i & \text{else}\end{cases} \tag{67}$$

where $\boldsymbol{X}_i^{\text{new, P2}}$ is the new status of the i^{th} zebra based on the second phase; and $F_i^{\text{new, P2}}$ is the fitness value of $\boldsymbol{X}_i^{\text{new, P2}}$.

The complete process of the ZOA involves initializing the population, updating the positions of the zebras through foraging phase and defense strategies, and refining the optimal solution after each iteration. In this study, we integrate the DDEA with the ZOA, and the overall algorithmic process is illustrated in Supplementary Material G Algorithm SG1.

Approaches for managing uncertainty and their practical applications in real-world contexts are illustrated in Supplementary Material H.

The input data of surrogate models based on tri-training algorithm consist of the incentive prices for each group, and the output data correspond to the resulting profits. Surrogate models based on the semi-supervised learning-based tri-training algorithm are used to replace the proposed bilevel optimization model, which are then integrated with the ZOA to form the proposed algorithm. The introduction of input and output data for surrogate models based on the tri-training algorithm is shown in Fig. 2.

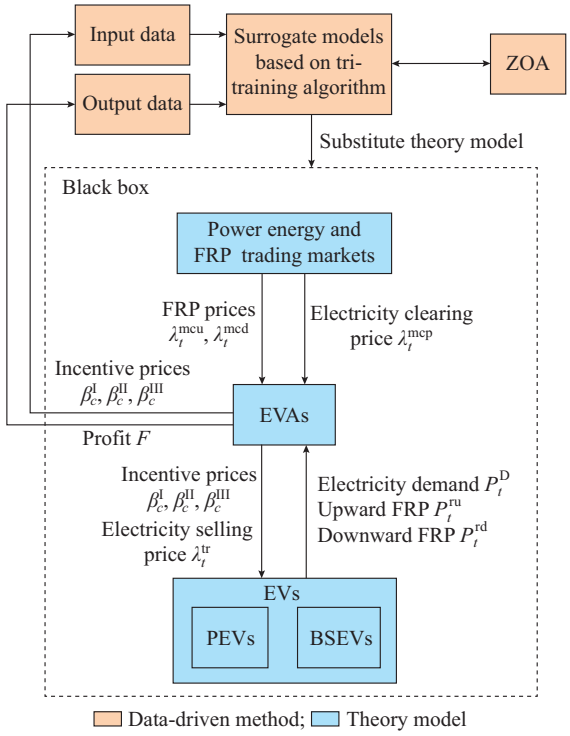

Fig. 2. Introduction of input and output data for surrogate models based on tri-training algorithm.

V. Case Study

The market clearing price and flexible ramping market price data used in the proposed bilevel optimization model are obtained from the Pennsylvania-New Jersey-Maryland (PJM) market in the United States [38]. The electricity selling price of the EVA is based on the PJM market price data, which are shown in Supplementary Material I Fig. SI1. A uniformly distributed random disturbance of ±5% is added to the electricity price to simulate price fluctuations in the actual electricity market. Details of the constant coefficients used are provided in Supplementary Material I Table SII.

A. Analysis of Power Flexibility of BSCSs

This study analyzes weekly charging data from a charging station in Hohhot, China. Given that the SOC range for both entry and depature data is [0, 1], a Beta distribution is used for the fitting. For the entry and depature data, the time data are first unified into integers in the range [1, 96], simulating 15 min charging intervals for each day, and a normal distribution is used for fitting. The corresponding distribution parameters are presented in Supplementary Material I Table SIII. A schematic of the EV entry time distribution is provided in Supplementary Material I Fig. SI2. The minimum SOC required to satisfy the next travel demand E_{ms} is randomly distributed between E_{start} and E_{exp}. Based on the fitted probability density function, the Monte Carlo method is used to obtain the data for 51 EVs.

To analyze the dispatchable range of a PEV cluster and charging modes with different incentive price groups, we set up multiple incentive price groups: incentive price group 1: $\beta_c^{I}=\$0.06$, $\beta_c^{II}=\$0.06$, $\beta_c^{III}=\$0.08$; incentive price group 2: $\beta_c^{I}=\$0.04$, $\beta_c^{III}=\$0.08$, $\beta_c^{III}=\$0.08$; incentive price group 3: $\beta_c^{I}=\$0.04$, $\beta_c^{III}=\$0.10$, $\beta_c^{III}=\$0.10$. The number of PEVs in different charging modes and with different incentive price groups is presented in Table I. The results of the feasible charging and discharging regions of PEV cluster under different incentive price groups are illustrated in Fig. 3.

TABLE I
Number of PEVs in Different Charging Modes and with Different Incentive Price Groups

Incentive price group	Number of PEVs		
	Mode I	Mode II	Mode III
1	43	8	0
2	0	50	1
3	3	14	34

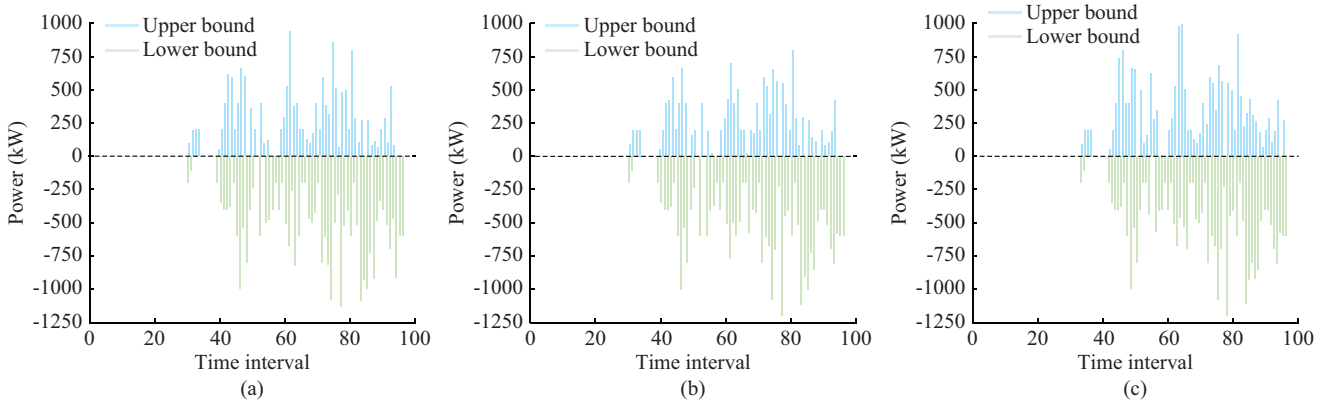

Fig. 3. Feasible regions of charging and discharging power of PEV cluster with different incentive price groups. (a) Incentive price group 1. (b) Incentive price group 2. (c) Incentive price group 3.

Table I shows that, as the incentive price for Mode II or Mode III increases, the number of PEVs that opt for the corresponding charging mode increases. Figure 3 shows that the downward flexible ramping dispatchable range is largely consistent across the three incentive price groups, whereas the upward flexible ramping dispatchable range for the first and second groups is smaller than that of the third group. This is because, although the maximum charging power of the PE-

Vs is the same across all three modes, the PEVs in Modes I and II are unable to discharge and can only reduce part of their charging power. Therefore, the upward flexible ramping dispatchable range for PEVs in Modes I and II is smaller than that in Mode III.

The feasible regions of charging and discharging power for the BSEVs are provided in Supplementary Material I Fig. SI3.

B. Feasibility and Accuracy Verification Analysis of Tri-training Algorithm

The algorithm settings used in this study are as follows. In the RBFN, the number of centroids is determined as the square root of the total number of training data points, and the radial propagation rate is set to be twice the average distance between centroids. The hidden-layer nodes in the RBFN are assigned based on the *k*-means clustering algorithm.

For the ZOA, the population size is set to be 100 with a maximum of 200 iterations, and the constant R is set to be 0.1. The probability of the population choosing the fleeing defense strategy or collective defense strategy is set to be 0.5. In this study, 100 incentive price groups are generated using the Latin hypercube sampling algorithm, and the corresponding profits for the EVAs are calculated using the bilevel optimization model proposed in Section III. The profits of EVs serve as the population fitness for the ZOA.

Various dataset sizes are used to evaluate the accuracy of the surrogate model. These datasets are split into training and testing sets in a ratio of 4:1 and are normalized.

Figure 4 shows the relative errors of the model integrated from three RBFN models (denoted as integrated model) for different dataset sizes. When the dataset size reaches approximately 100, the average relative error of the integrated model is less than 1.6%. As the dataset size increases to approximately 500, the relative error further decreases, with an average relative error of 0.7%, representing about a reduction of 56% compared with that with the dataset size of 100. This demonstrates that expanding the dataset size significantly enhances the prediction accuracy of the integrated model. When the dataset size reaches 1000, the average relative error decreases further, although the rate of improvement diminishes, indicating that the error tends to stabilize. The results suggest that the surrogate model trained by the semi-supervised learning-based tri-training algorithm can achieve satisfactory prediction results with a relatively small dataset.

Figure 5 shows the average relative errors of different models when the dataset size is 1000. The average relative error distributions of the integrated model and three surrogate models generally fall between 0.6% and 0.8%. Figure 6 illustrates the relative error ranges of the three surrogate models M_1-M_3 when the dataset size is 1000. The solid lines represent the mean relative errors of the three models, while the shaded areas indicate the fluctuation ranges of the errors across iterations. The minimum relative error of the three surrogate models is 0%, whereas the maximum relative error is approximately 2.8%. These relative errors are acceptable within the context of the ZOA, indicating that the surrogate models maintain stability and accuracy throughout the iterative process, which is essential for the ZOA to determine the optimal incentive prices based on the outputs of surrogate models.

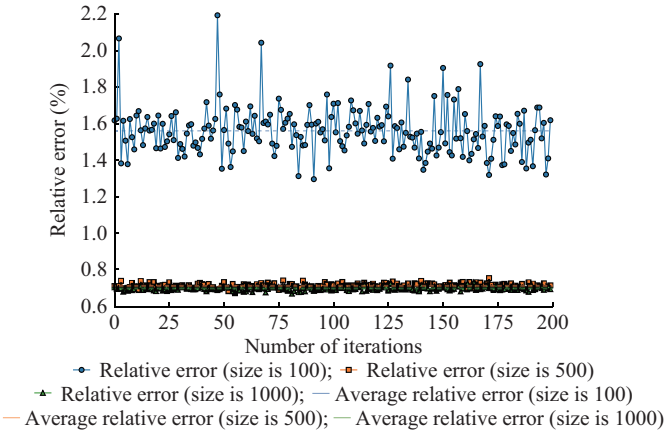

Fig. 4. Relative errors of integrated model for different dataset sizes.

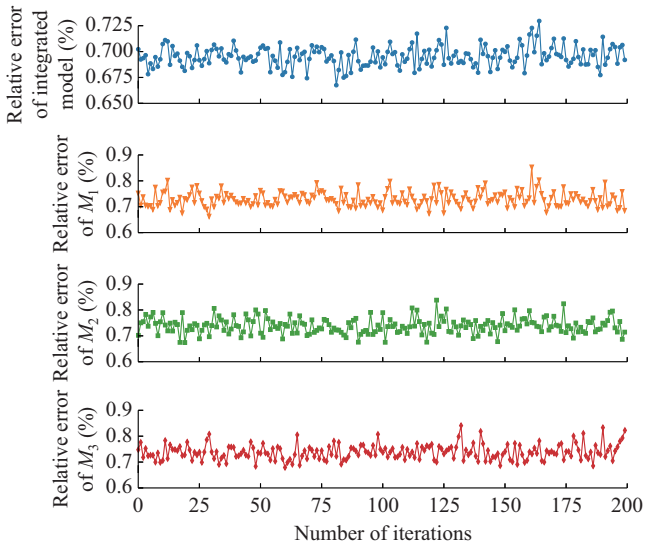

Fig. 5. Average relative errors of different models when dataset size is 1000.

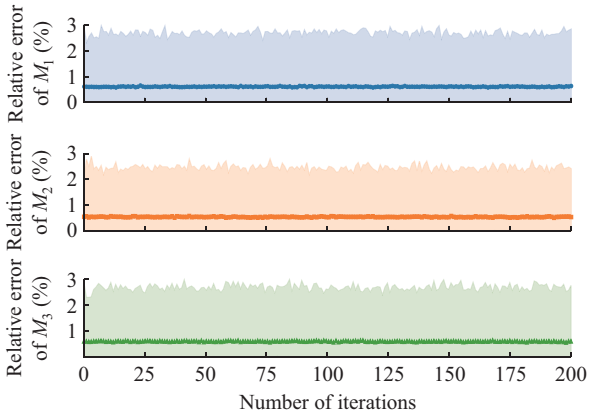

Fig. 6. Relative error ranges of three surrogate models when dataset size is 1000.

Experiments for evaluating the influence of electricity price uncertainty on model accuracy are provided in Supplementary Material I Fig. SI4. Additionally, experiments for

validating the superiority of the semi-supervised learning-based tri-training algorithm are presented in Supplementary Material I Figs. SI5 and SI6.

C. Performance Analysis of ZOA

In this subsection, 100 incentive price groups are generated using the Latin hypercube sampling algorithm to represent the zebra population. The individual dimension of the population is set to be 3, corresponding to the incentive price for each of the three modes. The maximum number of iterations is set to be 200, with the constants R and PR set to be 0.1 and 0.5, respectively. The incentive prices are normalized, with each dimension bounded to the range [0, 1]. A surrogate model is then employed to predict the profits of EVAs for random incentive prices. The predicted profits, normalized for consistency, are used as the fitness function in the ZOA. The surrogate model is trained with a dataset size of 1000.

We compare the GA, differential evolution (DE) algorithm, and PSO algorithm with the ZOA. The performance of the iterative optimization with different algorithms is shown in Fig. 7.

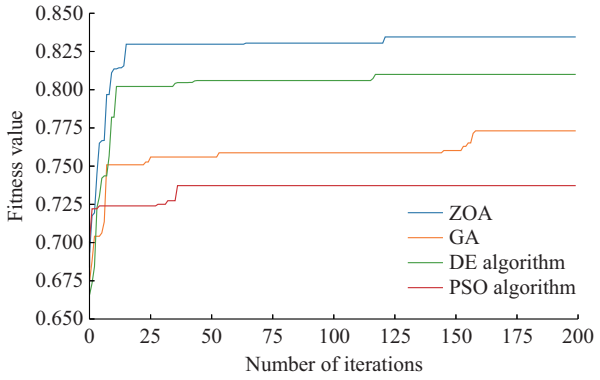

Fig. 7. Performance of iterative optimization with different algorithms

As shown in Fig. 7, the ZOA performs the best, with the blue curve stabilizing after approximately the 20th iteration, reaching a fitness value of 0.825, and maintaining stability thereafter. This indicates the excellent optimization efficiency and global search capability of the ZOA. The DE algorithm follows closely, with the green curve stabilizing at around the 20th iteration, achieving a final fitness value close to 0.800, which is slightly inferior to the ZOA in terms of performance. The GA and PSO algorithm perform relatively worse: the GA reaches a final fitness value of 0.775 after approximately 160 iterations, whereas the PSO algorithm only achieves a final fitness value of approximately 0.73, indicating limited optimization performance. In summary, the ZOA demonstrates an outstanding performance, exhibiting fast convergence and strong stability when tackling complex optimization problems. Compared with the other three algorithms, the ZOA converges to a better solution more rapidly during the iterative process and consistently maintains a high fitness value, highlighting its robust global search capability and reliability.

The optimal incentive prices obtained by the proposed algorithm are [0.045, 0.061, 0.110], at which the EVA achieves a profit of $2154. For comparison, when the incentive prices are set to be [0, 0, 0], the profit of the EVA is $2046, indicating that the incentive mechanism generates an additional revenue of $108. Experiments for validating the superiority of the proposed algorithm are provided in Supplementary Material I Fig. SI7.

VI. Conclusion

This study investigates a bidding method for EVAs to participate in the FRP trading market by utilizing a ZOA-based DDEA using a semi-supervised learning-based tri-training algorithm. This study is divided into three parts: a model for aggregating charging and swapping flexibility to capture the spatio-temporal operational characteristics of EVAs; a bilevel optimization model for the bidding of EVAs, which coordinates incentive pricing and charging strategies to balance the interests of EVAs and EVs in FRP trading, thereby enhancing the overall flexibility of EVAs; and a ZOA-based DDEA using a semi-supervised learning-based tri-training algorithm. The following conclusions can be drawn from the case studies.

1) The model that aggregates charging and swapping flexibility can provide a unified framework for representing the charging and swapping demands of PEVs and BSEVs in various scenarios.

2) Numerical tests demonstrate that introducing incentive prices in the bilevel optimization model can effectively increase the power flexibility of EVAs.

3) The proposed algorithm can leverage the integration of data-driven methods and semi-supervised learning to address the issues of high computational costs and limited data availability. The numerical tests indicate that the application of the semi-supervised learning-based tri-training algorithm improves the accuracy of the surrogate model while highlighting the superiority of the ZOA.

References

[1] S. Yu, H. Gui, and J. Yang, "China's provincial wind power potential assessment and its potential contributions to the 'dual carbon' targets," *Environmental Science and Pollution Research*, vol. 30, no. 5, pp. 13094-13117, Jan. 2023.

[2] S. Sreekumar, K. C. Sharma, and R. Bhakar, "Multi-interval solar ramp product to enhance power system flexibility," *IEEE Systems Journal*, vol. 15, no. 1, pp. 170-179, Mar. 2021.

[3] Jiemian News. (2025, Jan.). V2G charging pile resources incorporated into the North China power peak-shaving ancillary service market. [Online]. Available: http://www.chinapower.com.cn/dww/ddqc/20200422/16294.html

[4] National Energy Administration Shandong Supervision Office. (2025, Jan.). Notice on the issuance of the "Shandong Electric Power Ramp-up Auxiliary Service Market Trading Rules (Trial)". [Online]. Available: https://sdb.nea.gov.cn/dtyw/tzgg/202402/t20240208_245961.html

[5] X. Zhang, J. Hu, H. Wang *et al*., "Electric vehicle participated electricity market model considering flexible ramping product provisions," *IEEE Transactions on Industry Applications*, vol. 56, no. 5, pp. 5868-5879, Sept. 2020.

[6] Z. Wei, Y. Li, and L. Cai, "Electric vehicle charging scheme for a park-and-charge system considering battery degradation costs," *IEEE Transactions on Intelligent Vehicles*, vol. 3, no. 3, pp. 361-373, Sept. 2018.

[7] S. Li, P. Zhao, C. Gu *et al*., "Aging mitigation for battery energy storage system in electric vehicles," *IEEE Transactions on Smart Grid*, vol. 14, no. 3, pp. 2152-2163, May 2023.

[8] F. Alfaverh, M. Denaï, and Y. Sun, "Optimal vehicle-to-grid control for supplementary frequency regulation using deep reinforcement learning," *Electric Power Systems Research*, vol. 214, p. 108949, Jan. 2023.
[9] S. Cai and R. Matsuhashi, "Optimal dispatching control of EV aggregators for load frequency control with high efficiency of EV utilization," *Applied Energy*, vol. 319, p. 119233, Aug. 2022.
[10] C. Peng, J. Zou, and L. Lian, "Dispatching strategies of electric vehicles participating in frequency regulation on power grid: a review," *Renewable and Sustainable Energy Reviews*, vol. 68, pp. 147-152, Feb. 2017.
[11] N. K. Panda and S. H. Tindemans, "Efficient quantification and representation of aggregate flexibility in electric vehicles," *Electric Power Systems Research*, vol. 235, p. 110811, Oct. 2024.
[12] Y. Wen, Z. Hu, S. You *et al*., "Aggregate feasible region of DERs: exact formulation and approximate models," *IEEE Transactions on Smart Grid*, vol. 13, no. 6, pp. 4405-4423, Nov. 2022.
[13] M. Zhou, Z. Wu, J. Wang *et al*., "Forming dispatchable region of electric vehicle aggregation in microgrid bidding," *IEEE Transactions on Industrial Informatics*, vol. 17, no. 7, pp. 4755-4765, Jul. 2021.
[14] C. Wei, J. Xu, S. Liao *et al*., "Aggregation and scheduling models for electric vehicles in distribution networks considering power fluctuations and load rebound," *IEEE Transactions on Sustainable Energy*, vol. 11, no. 4, pp. 2755-2764, Oct. 2020.
[15] W. Meng, D. Song, L. Huang *et al*., "Distributed energy management of electric vehicle charging stations based on hierarchical pricing mechanism and aggregate feasible regions," *Energy*, vol. 291, p. 130332, Mar. 2024.
[16] J. Jian, M. Zhang, Y. Xu *et al*., "An analytical polytope approximation aggregation of electric vehicles considering uncertainty for the day-ahead distribution network dispatching," *IEEE Transactions on Sustainable Energy*, vol. 15, no. 1, pp. 160-172, Jan. 2024.
[17] Y. Tao, J. Qiu, and S. Lai, "Deep reinforcement learning based bidding strategy for EVAs in local energy market considering information asymmetry," *IEEE Transactions on Industrial Informatics*, vol. 18, no. 6, pp. 3831-3842, Jun. 2022.
[18] M. J. Salehpour and M. J. Hossain, "Leveraging machine learning for efficient EV integration as mobile battery energy storage systems: exploring strategic frameworks and incentives," *Journal of Energy Storage*, vol. 92, p. 112151, Jul. 2024.
[19] X. Xu, Z. Zhan, Z. Mi *et al*., "An optimized decision model for electric vehicle aggregator participation in the electricity market based on the Stackelberg game," *Sustainability*, vol. 15, no. 20, p. 15127, Oct. 2023.
[20] M. Kiannejad, M. R. Salehizadeh, and M. Oloomi-Buygi, "Two-stage ANN-based bidding strategy for a load aggregator using decentralized equivalent rival concept," *IET Generation, Transmission & Distribution*, vol. 15, no. 1, pp. 56-70, Jan. 2021.
[21] D. Liu, L. Wang, M. Liu *et al*., "Optimal energy storage allocation strategy by coordinating electric vehicles participating in auxiliary service market," *IEEE Access*, vol. 9, pp. 95597-95607, Jul. 2021
[22] B. Shakerighadi, A. Anvari-Moghaddam, E. Ebrahimzadeh *et al*., "A hierarchical game theoretical approach for energy management of electric vehicles and charging stations in smart grids," *IEEE Access*, vol. 6, pp. 67223-67234, Nov. 2018
[23] C. Lou, C. Li, L. Zhang *et al*., "Two-stage bidding strategy with dispatch potential of electric vehicle aggregators for mitigating three-phase imbalance," *Journal of Modern Power Systems and Clean Energy*, vol. 13, no. 5, pp. 1823-1835, Sept. 2025.
[24] R. Mohammadi, H. R. Mashhadi, and M. Shahidehpour, "Market-based customer reliability provision in distribution systems based on game theory: a bi-level optimization approach," *IEEE Transactions on Smart Grid*, vol. 10, no. 4, pp. 3840-3848, Jul. 2019.
[25] P. Sheikhahmadi, S. Bahramara, A. Mazza *et al*., "Bi-level optimization model for the coordination between transmission and distribution systems interacting with local energy markets," *International Journal of Electrical Power & Energy Systems*, vol. 124, p. 106392, Jan. 2021.
[26] M. Setak, F. Feizizadeh, H. Tikani *et al*., "A bi-level stochastic optimization model for reliable supply chain in competitive environments: hybridizing exact method and genetic algorithm," *Applied Mathematical Modelling*, vol. 75, pp. 310-332, Nov. 2019.
[27] A. Sinha, T. Soun, and K. Deb, "Using Karush-Kuhn-Tucker proximity measure for solving bilevel optimization problems," *Swarm and Evolutionary Computation*, vol. 44, pp. 496-510, Feb. 2019.
[28] Y. Jin, H. Wang, T. Chugh *et al*., "Data-driven evolutionary optimization: an overview and case studies," *IEEE Transactions on Evolutionary Computation*, vol. 23, no. 3, pp. 442-458, Jun. 2019.
[29] P. Huang, H. Wang, and Y. Jin, "Offline data-driven evolutionary optimization based on tri-training," *Swarm and Evolutionary Computation*, vol. 60, p. 100800, Feb. 2021.
[30] Z. Zhou, Y. S. Ong, M. H. Nguyen *et al*., "A study on polynomial regression and Gaussian process global surrogate model in hierarchical surrogate-assisted evolutionary algorithm," *IEEE Congress on Evolutionary Computation*, vol. 3, no. 3, pp. 2832-2839, Sept. 2005.
[31] Y. Jin, M. Olhofer, and B. Sendhoff, "A framework for evolutionary optimization with approximate fitness functions," *IEEE Transactions on Evolutionary Computation*, vol. 6, no. 5, pp. 481-494, Oct. 2002.
[32] L. Willmes, T. Back, Y. Jin *et al*., "Comparing neural networks and Kriging for fitness approximation in evolutionary optimization," in *Proceedings of 2003 Congress on Evolutionary Computation*, Canberra, Australia, Jul. 2004, pp. 663-670.
[33] Y. Jin and B. Sendhoff, "Reducing fitness evaluations using clustering techniques and neural network ensembles," in *Proceeding of Genetic and Evolutionary Computation Conference*, Seattle, USA, Jun. 2004, pp. 688-699.
[34] R. G. Regis, "Evolutionary programming for high-dimensional constrained expensive black-box optimization using radial basis functions," *IEEE Transactions on Evolutionary Computation*, vol. 18, no. 3, pp. 326-347, Jun. 2014.
[35] C. Sun, Y. Jin, J. Zeng *et al*., "A two-layer surrogate-assisted particle swarm optimization algorithm," *Soft Computing*, vol. 19, no. 6, pp. 1461-1475, Jun. 2015.
[36] C. Sun, Y. Jin, R. Cheng *et al*., "Surrogate-assisted cooperative swarm optimization of high-dimensional expensive problems," *IEEE Transactions on Evolutionary Computation*, vol. 21, no. 4, pp. 644-660, Aug. 2017.
[37] G. Li and J. Shi, "On comparing three artificial neural networks for wind speed forecasting," *Applied Energy*, vol. 87, no. 7, pp. 2313-2320, Jul. 2010.
[38] PJM. (2024, Oct.). Real-time energy market locational marginal pricing in PJM. [Online]. Available: http://dataminer2. pjm. com/feed/rt_hrl_lmps/definition

Xu Wang received the B.S. degree in electrical engineering from Southeast University, Nanjing, China, in 2010, and the Ph.D. degree from Shanghai Jiao Tong University, Shanghai, China, in 2016. From 2016 to 2018, he was a Postdoctoral Associate with the Robert W. Galvin Center for Electricity Innovation, Illinois Institute of Technology, Chicago, USA. He is currently an Associate Professor with the Key Laboratory of Control of Power Transmission and Conversion, Shanghai Jiao Tong University. His research interests include resilient power system, renewable energy, power system economics and optimization.

Hanxiao Wu received the B.S. degree in electrical engineering from Shanghai Jiao Tong University, Shanghai, China, in 2023. He is currently pursuing the M.S. degree in electrical engineering at Shanghai Jiao Tong University, Shanghai, China. His research interests include resilient power system, power system optimization, and electricity market.

Guanxun Diao received the B.S. degree in electrical engineering and automation and the M.S. degree in electrical engineering from Tsinghua University, Beijing, China, in 2002 and 2005, respectively. He began his professional career in August 2005 and has been engaged in the management and maintenance of ultra-high voltage (UHV) and direct current (DC) transmission systems. Since March 2015, he has served as the Director of the UHV and DC Transportation Center of the Inspection and Maintenance Branch at the State Grid Shanghai Municipal Electric Power Company, Shanghai, China. His research interests include UHV power transmission, DC transmission system, and intelligent maintenance of power equipment.

Chen Fang received the B.S. and Ph.D. degrees in electrical engineering from Tsinghua University, Beijing, China, in 2006 and 2011, respectively. He is currently a Senior Professional Electrical Engineer with the Electric Power Research Institute, State Grid Shanghai Municipal Electric Power Company, Shanghai, China. His research interests include electric energy storage system and electric vehicle-grid interaction.

Canbing Li received the B.E. and Ph.D. degrees from the Department of Electrical Engineering, Tsinghua University, Beijing, China, in 2001 and 2006, respectively. He is currently a Professor with Shanghai Jiao Tong University, Shanghai, China. His research interests include power system, smart grid, renewable energy, with an emphasis on large-scale power system dispatch, economic and secure operation of power systems, energy efficiency

and energy saving in smart grid, electric demand management of data centers, and vehicle-to-grid technology.

Kai Gong received the B.S. degree in electrical engineering from Huazhong University of Science and Technology, Wuhan, China, in 2017, and the Ph. D. degree from Shanghai Jiao Tong University, Shanghai, China, in 2022. He is currently a Postdoc in control science and engineering with Zhejiang University, Hangzhou, China. His research interests include optimal operation of battery energy storage system, resilient power system, and power system optimization.

Chuanwen Jiang received the M.S. and Ph.D. degrees from the Huazhong University of Science and Technology, Wuhan, China, in 1996 and 2000, respectively. He is currently a Professor with the School of Electrical Engineering, Shanghai Jiao Tong University, Shanghai, China. His research interests include reservoir dispatch, power system analysis, electricity market, and power system economics and optimization.

Wentao Huang received the Ph. D. degree in electrical engineering from Shanghai Jiao Tong University, Shanghai, China, in 2015. He is currently a Professor with the School of Electrical Engineering, Shanghai Jiao Tong University. His research interests include protection and control of active distribution network, microgrid, smart grid, and renewable energy.

Shenxi Zhang received the B.S. degree in electrical engineering from Hohai University, Nanjing, China, in 2011, and the Ph.D. degree in electrical engineering from Shanghai Jiao Tong University, Shanghai, China, in 2016. He is currently a Professor with Shanghai Jiao Tong University. His research interests include power system optimization, renewable generation, and integrated energy system.